Flood Extent Mapping in the Caprivi Floodplain Using Sentinel-1 Time Series

Tsitsi Bangira, Lorenzo Iannini, Massimo Menenti, Adriaan van Niekerk, and Zoltan Vekerdy

***Abstract*—Deployment of Sentinel-1 (S1) satellite constellation carrying a C-band synthetic aperture radar (SAR) enables regular and timely monitoring of floods from their onset until returning to nonflooded (NF) conditions. The major constraint on using SAR for near-real-time (NRT) flood mapping has been the inability to rapidly process the obtained imagery into reliable flood maps. This study evaluates the efficacy of S1 time series for quantifying and characterizing inundation extents in vegetated environments. A novel algorithm based on statistical time-series modeling of flooded (F) and NF pixels is proposed for NRT flood monitoring. For each new available S1 image, the probability of temporarily F conditions is tested against that of NF conditions by means of likelihood ratio tests. The likelihoods for the two conditions are derived from early acquisitions in the time series. The algorithm calibration consists of adjusting two likelihood ratio thresholds to match the reference F area extent during a single flood season. The proposed algorithm is applied to the Caprivi region, the resulting maps were compared to cloud-free Landsat-8 (LS8) derived maps captured during two flood events. A good spatial agreement (85–87%) between LS8 and S1 flood maps was observed during the flood peak in both 2017 and 2018 seasons. Significant discrepancies were noted during the flood expansion and recession phases, mainly due to different sensitivities of the data sources to the emerging vegetation. Overall, the analysis shows that S1 can stand as an effective standalone or gap-filling alternative to optical imagery during a flood event.**

***Index Terms*—Floating and emergent vegetation, flood mapping, land cover (LC), synthetic aperture radar (SAR), Sentinel-1 (S1), time series.**

Manuscript received November 3, 2020; revised January 29, 2021, March 30, 2021, and May 12, 2021; accepted May 12, 2021. Date of publication May 25, 2021; date of current version June 9, 2021. This work was supported by the European Space Agency in the framework of the ALCANTARA Program, which includes Stellenbosch University and TU Delft University under Grant 4000112465/ 14/F/MOS 14-P11. *(Tsitsi Bangira and Lorenzo Iannini contributed equally to this work.) (Corresponding author: Tsitsi Bangira.)*

Tsitsi Bangira is with the Department of Geography and Environmental Studies, Stellenbosch University, Stellenbosch 7602, South Africa, and also with the Department of Civil Engineering and Geosciences, Delft University of Technology, 2628 CD Delft, The Netherlands (e-mail: tsitsibangira@gmail.com).

Lorenzo Iannini is with the Department of Civil Engineering and Geosciences, Delft University of Technology, 2628 CD Delft, The Netherlands (e-mail: L.Iannini@tudelft.nl).

Massimo Menenti is with the Department of Civil Engineering and Geosciences, Delft University of Technology, 2628 CD Delft, The Netherlands, and also with the State Key Laboratory of Remote Sensing Science, Institute of Remote Sensing and Digital Earth, Chinese Academy of Sciences, Beijing 100864, China (e-mail: m.menenti@tudelft.nl).

Adriaan van Niekerk is with the Department of Geography and Environmental Studies, Stellenbosch University, Stellenbosch 7602, South Africa (e-mail: avn@sun.ac.za).

Zoltan Vekerdy is with the Faculty of Geo-Information Science and Earth Observation, University of Twente, 7500 NB Enschede, The Netherlands, and also with the Faculty of Agricultural and Environmental Sciences, Szent István University, 2100 Gödöllő, Hungary (e-mail: z.vekerdy@utwente.nl).

Digital Object Identifier 10.1109/JSTARS.2021.3083517

I. Introduction

RIPARIAN areas, such as the Caprivi flood plain, are flooded (F) almost every year due to excess rainfall in the upper catchments [1]. Riverine flooding affects the ecological (e.g., ecosystem productivity, species distribution and occurrence, nutrients, and sediment dynamics) and socioeconomic systems (e.g., causing loss of life, waterborne diseases, destruction of shelter, and infrastructure damage). Obtaining detailed information at regional scales is deemed fundamental to guide the identification of flood prone areas and to mitigate flood hazards [2], [3]. *In situ* observations of flooding are severely limited by the inaccessibility of such areas due to flooding, poor road infrastructure, wet soils, and dense vegetation. However, remote sensing techniques that make use of synthetic aperture radar (SAR) and multispectral data have been widely recognized as an alternative method for mapping floods in near real time (NRT) over large geographical and inaccessible areas [3], [4].

Multispectral imagery is easily interpretable, and the extraction of open water from such data is relatively straightforward [5]. However, cloud conditions can limit their application for flood monitoring. In contrast, SAR sensors have all-weather as well as day–night imaging capabilities [6]. Furthermore, SAR has been shown to penetrate vegetation canopies to an extent depending on canopy density, wavelength, and polarization, which helps to observe surface water partly obscured by vegetation [7]–[9].

SAR data have been successfully used for flood mapping in a number of studies [2], [10]–[13]. These studies focused on detecting open water, assuming perfectly smooth surfaces of high dielectric constants that reflect most of the radiation away from side-looking SAR sensors. Open water regions were, thus, identified as regions of low backscatter, appearing dark in the image. This approach successfully delineates open water in most cases, but the presence of emergent vegetation and waves caused by wind can increase backscatter to such an extent that inundated areas are confused with dry land surfaces [7], [8]. Emergent vegetation is when trees, grass, shrubs, and crops are F or partially F. The amount of microwave energy scattered off an object is mainly a function of its surface roughness, with morphology and dielectric properties as subsidiary factors [14]. The interaction between the SAR signal and the vegetation occurs through two main mechanisms. The first is a direct reflection from the plant structure and the canopy, generating so-called volume scattering. The second is a result of multiple reflections from the horizontal surface (ground or water) and vertical structures (trunks or stems), producing so-called

double-bounce scattering. Therefore, the fraction of vegetation in a given pixel has a significant impact on the SAR signal [15]. This makes flood detection in vegetated areas more challenging than for open water features.

Recently, there have been significant improvements in SAR-based algorithms for mapping flooded vegetation (FV) [3], [7], [9], [16]–[18]. The commonality of these algorithms is that they all make use of thresholding to initialize the classification process. However, the accuracy of thresholding dramatically varies depending on the land cover (LC) characteristics (e.g., rough soil surface, vegetation, and open water) within the scene. Theoretical electromagnetic backscattering models have traditionally been used to define appropriate threshold values for mapping FV [19]. However, such approaches require detailed soil, vegetation, and LC maps, which are often unavailable to accurately estimate thresholds. There is, thus, a need for approaches that automatically determine the optimal threshold value for a scene without the need for ancillary data or operator intervention. Such techniques must take double bouncing caused by vegetation and the diffuse backscatter from dry and bare surfaces into consideration. A previous study [20] pioneered an approach that applied a split-based automatic thresholding procedure on TerraSAR-X data for NRT flood detection. A similar approach was taken by Matgen *et al.* [21], where a nonlinear fitting algorithm under the gamma distribution assumption was used to determine a suitable threshold to model F areas. Although these studies achieved overall accuracies of more than 80%, they are computationally expensive and time consuming, which limits their application to operational and NRT flood mapping for large and complex areas.

More work is needed to delineate inundated areas and FV in NRT using Sentinel-1 (S1). Automatic processing chains based on thresholding are ideal for rapid flood mapping and for improving the delivery time of emergency information. The study done by Twele *et al.* [3] proposed an automated S1-based processing chain for detecting and monitoring floods in NRT. The algorithm was applied to a single SAR image to detect open water. Although a single SAR image can provide a reasonable estimate of the flood extent, setting a threshold for flood probability based on one image is risky and inflexible, especially in vegetated flood plains as local variations in LC are difficult to deduce from a single image. However, temporal changes in backscatter can be determined from a series of SAR images. Moreover, single images do not reveal the abrupt change in the intensity of backscatter values caused by FV [22]. However, by analysing a series of SAR images additional information, such as temporary FV; vegetation that is partially covered with water after heavy rains or during a flood event can be extracted [23].

This study presents a rapid, simple, and semiautomated pixel-based technique for mapping open water, temporary open water, and FV over a large and complex region based on abrupt changes occurring on the latest image. The threshold backscatter values for identifying these phenomena are computed from the global and local gray-level histograms of the SAR data using the popular and versatile Otsu algorithm [24]. In contrast to previous studies [22], [23], the proposed method is based on S1 time series only and does not require any ancillary data such as river levels and LC. For each new available image, the probability of F conditions is estimated using the observations from the previous images and is tested against the probability of wet conditions. A pixel-adaptive modeling and testing procedure is applied to the cross-polarized backscatter VH and to the polarization ratio VH/VV. Operator intervention is only needed during the algorithm setup, where the desired balance between false flood positives and negatives must be specified.

II. Materials

A. Study Area

The proposed technique was evaluated in the Caprivi floodplain, located in the northeastern part of Namibia (see Fig. 1). The Caprivi floodplain is an extensive flat sand-filled part of the Kalahari basin with elevations ranging from 950 to 980 meters above sea level [25]. The floodplain is complex and surrounded by four rivers, namely, the Zambezi (fourth longest river in Africa), Cuando/Kwando, Linyanti, and Chobe [26], [27]. These rivers have different hydrological regimes with diverse habitats, vegetation, and aquatic life [28]. The Zambezi River has a typical autumn flood regime, with a peak flow from March to May. The Chobe River flows in a southwestern direction, when the Zambezi River starts flooding and changes direction toward the Zambezi (northeast) when the levels of the Zambezi start subsiding. The Kwando and Linyanti Rivers normally flood in June and July, respectively [26].

The Caprivi floodplain is a typical savannah ecosystem, consisting of sparsely distributed impalila, riverine, mopane, and Kalahari woodlands interspersed with open thick-stemmed grasslands [25]. The main economic activity of the area is tourism, subsistence agriculture, and commercial fishing. The Caprivi people have adapted to the flooding cycles by migrating to temporary accommodation in elevated campsites (established by the government) during the wet season. When the floodwater recedes, the communities return to their homes to continue with their agricultural activities.

B. In Situ Data Collection

In situ observations (see Fig. 1, right) were collected using a handheld Trimble differential global positioning system (GPS) receiver with submeter accuracy. The GPS recordings were taken using a boat to identify the locations of areas with different vegetation types and flood levels during the flood event. The field surveys were conducted from April 4 to 7 2017. The samples were identified prior to the field survey and stratified according to LC (some samples were found to be inaccessible during the field survey). The visited locations were recorded and were used to extract spectral data and backscatter (dB) values from Landsat-8 (LS8) and S1 data, respectively. The major LC classes observed at the sampled locations were dry soil, temporary open water, open water, FV, and nonflooded (NF) vegetation. Redundant observations were deleted resulting in a total of 725 samples, 125 for each LC type. The samples were also labeled as F and NF.

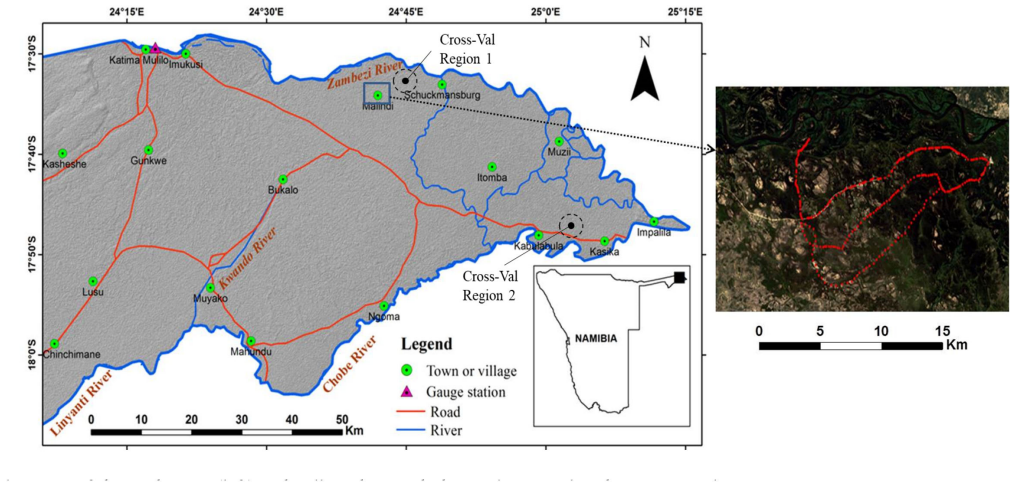

Fig. 1. Location map of the study area (left) and collected ground observations overlayed on a true color Landsat-8 image from April 10, 2017 (right).

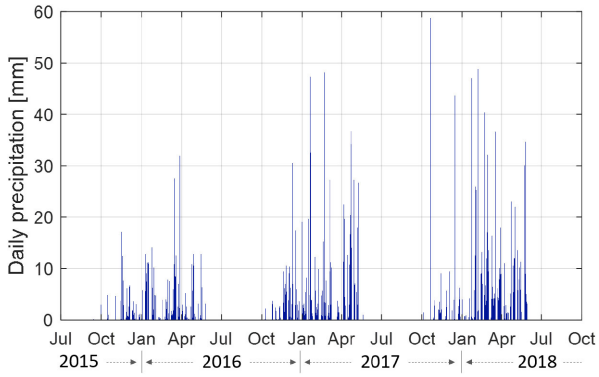

Fig. 2. Rainfall events in the Caprivi floodplain from July 2015 to October 2018.

Fig. 2 shows the rainfall records in the Caprivi floodplain at Katima Mlilo (see Fig. 1) for the period July 1 2015 to October 31 2018, based on data from the integrated multisatellite retrievals for global precipitation measurement mission. The figure shows that rainfall started around mid-October and ended in early April over the two years.

The peak rainfall occurs between January and March, whereas as shown by the analysis in Section V, the flood peaks occur in either April or May. Therefore, the floods in Caprivi are not a result of excessive rainfall received in the area. It is mainly because the large volumes of upstream water break the banks of the Zambezi River toward the end of the rainy season.

C. Remote Sensing Data Collection

For the period from December 2016 to September 2018, the test area is covered by 55 images of S1 interferometric wide swath acquisitions with a regular sampling of 12 days. Only one satellite (Sentinel-1B) in the ascending orbit (6 P.M. local time) is active over the region. The Ground Range Detected (GRD) products were used for the study. Such products provide the intensities in digital number (DN) format that is calibrated and processed to obtain the radar cross section per meter square on the ground, commonly referred to as the sigma nought (σ_0) or the normalized radar cross section (NRCS). As outlined in Table I, the images have a spatial ground resolution of 20 $\times$ 22 m (ground range $\times$ azimuth) after multilooking with an estimated equivalent number of looks of 4.4. Both the VH- and the VV-polarized images underwent the same standard preprocessing operations, as described in Section IV-A. The study area is illuminated with incidence angles ranging from 33° to 39°. It is assumed that the impact of the six-degree difference on the backscatter is negligible.

TABLE I
OUTLINE OF THE SENTINEL-1 AND LANDSAT-8 OLI DATASETS USED FOR THE STUDY

SENTINEL-1	
Satellite	Sentinel-1B
Mode	Ascending
Acquisition time	6 PM
Incidence angles	33° - 36°
Product	Ground Range Detected
Resolution	20 m (azimuth) x 5 m (ground range)
Number of images	52 (January 2017 - September 2018)

LANDSAT-8	
Instrument	OLI
Acquisition time	10 AM
Product	USGS Surface Reflectances
Resolution	30 m
Cloud Coverage	$<$ 40 %
Number of images	27 (February 2017 - August 2018)

The dates of the S1 and LS8 acquisitions used are reported in Fig. 3. The S1 images of March 25, April 6, May 12, and June 29, 2017 and their associated cloud-free LS8 acquisitions (with exact match except for the image acquired on April 10) are highlighted as they are adopted for calibrating the algorithm during the flood expansion (first two pairs) and flood recession (last two pairs) phase. The two images at the beginning of April (S1 at April 6 and LS8 at April 10) are used for the validation

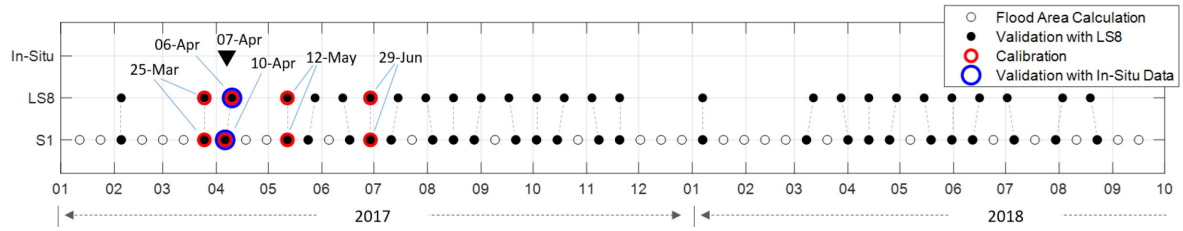

Fig. 3. Acquisition dates of S1 and LS8 used in the study. The *in situ* data collection is also reported. All the S1 images have been fed to the flood mapping algorithm. The markers indicate which S1 and LS8 acquisitions have been used for cross validation, for algorithm calibration, and for the validation with the *in situ* data.

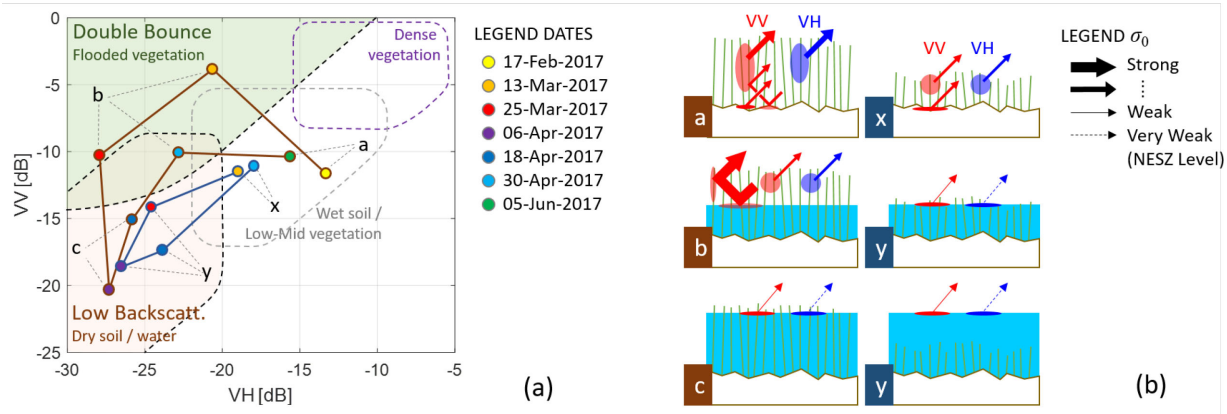

Fig. 4. (a) S1 time series for two vegetated locations before, during, and after the 2017 flood event in Caprivi. The simplified boundaries for the most significant scattering mechanisms occurring in the flood plain are also represented in the VH and VV planes. The first location (brown line) shows the signal of tall grass and shrubs, whereas the second (blue line) is for short grass. The colored markers convey temporal information. In the first location, the flooding period started earlier and ended later than in the second location. (b) Sketched representation of the scattering mechanisms for the different LC types and different flood levels. Note that the scenarios **c** and **y** essentially produce the same mechanism types. The double-bounce reflection from the soil–canopy and soil–water interaction in VV are indicated by the three-segment arrows in **a** and **b**, respectively.

with the *in situ* measurements as they were acquired during the field survey.

III. Backscatter Analysis

The interaction of water with vegetation and soil changes the nature and intensity of the SAR polarimetric mechanisms [29]. Although this study focuses on the Caprivi region, similar trends can be observed in regions with similar climate, landscape morphology, vegetation type, and vegetation distribution. During the onset of the rainy season (from November to February), the backscatter gradually increases in both the copolarized (VV) and cross-polarized (VH) channels, as the plants develop and the water content increases in the soil and in the canopy. The occurrence of a flood event manifests itself in the radar imagery through abrupt changes in the amplitude or/and in the type of the scattering mechanisms [30]. Such changes are LC dependent.

Short and sparsely distributed vegetation has a different backscatter pattern compared to dense distributed taller grass or shrubs, as illustrated in Fig. 4. Short vegetation [see blue line in Fig. 4(a)] experiences a sudden drop in both the VH and VV intensities as soon as the soil is inundated. The decrease in VH is typically higher as large portions of the canopy responsible for most of the cross-polarized reflected signal (volume scattering) are quickly lost below the water level. On average, the values of VV are significantly lower than preflood values. However, the response of VV is more variable than that of VH. This is mainly due to the higher sensitivity of the copolarized signal to surface scattering. The roughness of the water surface due to wind-blown waves (Bragg and non-Bragg effects) [31] likely compensates, at least partly, for the loss of the canopy scattering [32]. It is also assumed, within our definition of short vegetation, that no significant enhancement effects are expected from the interaction of the field with the canopy and with the water surface. This implies that the plant elements (stems, sheaths, blades, and leaves) are thin or short enough compared to the radar wavelength (5 cm in the S1 case).

In the case of tall vegetation, with vertically oriented elements in the plant geometric structure, a more diverse temporal trajectory can be expected [see, as an example, the red line in Fig. 4(a)]. In dry conditions, most of the reflected signal can be typically attributed to the direct interaction of the field and the canopy. However, as shown in panel **a** of Fig. 4(b), when the incident wave is not fully obstructed by the vegetation layer, a smaller portion of the backscatter in the copolarized bands can be attributed to rough surface scattering from the soil

and multiple bounce scattering from soil–canopy interaction. The soil–canopy mechanisms prevail over the direct surface scattering when the soil surface is smooth. Contrary, the balance is reversed for very rough soils. During the inundation, both copolarized (HH and VV) and cross-polarized channels (HV and VH) experience a loss in the volume backscatter, as the canopy is gradually submerged. When the signal penetrates the canopy and touches the water surface, however, this loss is partly or fully compensated in the copolarized backscatter by the inception of water–plant/plant–water interaction mechanisms that can even produce NRCS enhancements with respect to the preflood levels [7], [8]. The cross-polarized returns are instead significantly less influenced by such double-bounce effects, as shown in panel **b** of Fig. 4. Such contrasting behavior in the two channels provides the rationale for using the VH/VV ratio for mapping FV. For grasses and sparse shrubs, which is the dominant vegetation in semiarid areas, the increase in VV typically occurs at the beginning of the flood event when the water is shallow [see red-colored line in Fig. 4(a)]. The VV NRCS drops to bare ground or lower levels when the water is high enough to submerge most of the plant structure (in case of calm or light wind). The cross-polarized backscatter can get to and even fall below the noise equivalent sigma nought (NESZ) power in the case of an open and smooth water surface. However, due to the removal of the thermal noise bias [33] in the preprocessing phase, such levels are, however, still significant. In such F conditions, the VH channel is the most suited indicator for detecting the presence of "open" water, due to the aforementioned sensitivity of VV to surface roughness [34]. In support of these considerations and further assisted by Fig. 4, four different imaginary regions in the dual polarization backscatter domain can be identified for semiarid (not impervious) areas:

1) an FV region characterized by double-bounce mechanisms and hence by VH/VV < -10 dB;
2) a region associated with open water and dry soil with very low VH (< -20 dB) and VV (< -15 dB) NRCS. The larger range of values potentially spanned by VV with respect to VH shall be attributed to the variability in the surface roughness conditions;
3) a moderate backscatter region with VH and VV NRCS values fluctuating. This includes a variety of LC conditions such as vegetated surfaces (grasses, shrubs, and crops) and wet bare soil;
4) a dense vegetation region characterized by high VH (> -15 dB) and high VV (> -10 dB) NRCS.

In view of such analysis, both the cross-polarization and copolarization intensities as well as their temporal trajectories are essential for delineating and mapping FV.

IV. Methodology

Based on the conceptual analysis presented in the previous sections, a novel approach for the continuous monitoring of floods, from their onset until the return to NF conditions, is proposed. The mapping algorithm is entirely based on S1 data, whereas its calibration is based on one or more flood maps during both the flood expansion and the flood recession phases. In this article, two maps for each phase were used, derived from optical (LS8) images. The proposed validation phase accounts for a comparison with the optical-derived maps on multiple flood seasons and an absolute accuracy evaluation with the *in situ* data. The use of digital elevation models (DEMs), a common ancillary data source for spatial flood constraining, was not considered since the Caprivi floodplain is extremely flat, with an estimated total elevation range of 28 m over a 3000-km^2 area. As conveyed by the flowchart in Fig. 5, when a new S1 product is available at time t, a new processing cycle or iteration is carried out. The cycle receives the following as inputs:

1) the preprocessed VH and VV images at time t;
2) the stack of the past L images;
3) the intermediate products generated by the previous iteration at time $t-1$, comprising the land and water signature models (discussed in Section IV-B);
4) the previous flood map output.

Each cycle involves preprocessing, modeling, and classification phases. The modeling and classification steps, highlighted by the blue-colored frame in the flowchart, are applied independently to the cross-polarized backscatter, $\sigma_{0,VH}$, and to the polarization ratio, $\frac{\sigma_{0,VH}}{\sigma_{0,VV}}$. Although not explicitly reported in Fig. 5, two distinct sets of intermediate products are, thus, returned at the end of each iteration. The reader should also be aware that the models and the mathematical expressions reported in the next subsections are based on a logarithmic scale (dB values).

A. Preprocessing

The S1 VH and VV GRD products are radiometrically calibrated, unbiased from the thermal noise, terrain-corrected, and projected to a geographic coordinate system using the sentinel application platform. The two polarization channels are speckle filtered by applying a refined Lee sigma filter [35]. Speckle filtering reduces the speckle noise and leads to a spatially and temporally smooth image, depending on the areas' homogeneity. The polarization ratio (in dB) is computed through simple band subtraction.

B. Modeling

For every up-to-date image at time t, the observed pixel feature, y_t, is tested against two probability models: 1) a dry/NF land model and 2) an F land model. The model parameters are predicted from the previous observations, and hence, they are computed at time $t-1$. Simple unimodal Gaussian distributions have been adopted for both models. The outcome of the testing procedure, illustrated in Section IV-C, are binary maps with pixels labeled as either NF or F.

1) NF Model: The observed feature of a generic pixel in NF conditions at time t is described by

$$y_t \sim \mathcal{N}(\mu_t, \nu_t) \tag{1}$$

with μ_t and ν_t being the theoretical mean and variance of the probability density function (PDF) model, respectively. The generic nomenclature y_t can represent either VH or the ratio VH/VV, expressed in dB. Extreme values are closer together in

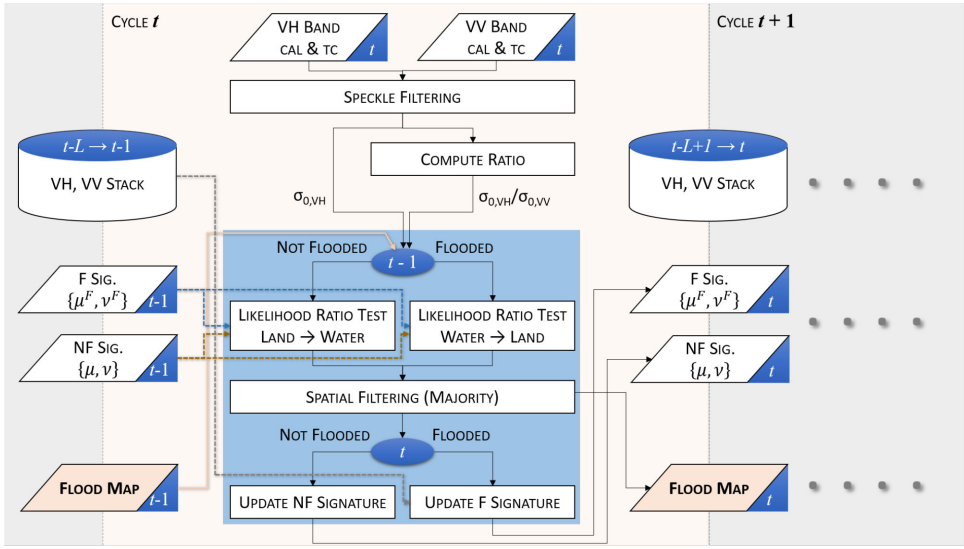

Fig. 5. Flowchart for the cycle/iteration t of the flood mapping algorithm. The blue-colored frame represents the processing block that is identically applied to both the VH and VH/VV inputs. Note as well that the flowchart does not include the map fusion step, which shall follow as a simple external postprocessing.

the logarithmic scale; therefore, the logarithmic scale provides a closer adherence to the model than the linear one. This can be specifically observed when the Chi-square distribution of the radar cross section rapidly tends to log-normality with the increasing number of looks. The set of L previous observations is defined as

$$\mathbf{y}_t = \{y_n,\ n = (t-L), \ldots, (t-1)\} \tag{2}$$

where the observed feature at time t is not included.

The observation set can be further extended to a spatial neighborhood Ω of the pixel

$$\mathbf{Y}_t = \{\mathbf{y}_t,\ \forall\, \text{pixel} \in \Omega\}\,. \tag{3}$$

Assuming a static process, the NF distribution parameters can be estimated from the samples in (2) and (3) by means of

$$\hat{\mu}_t = \langle \mathbf{y}_t \rangle \tag{4}$$

$$\hat{\nu}_t = \text{var}(\mathbf{Y}_t) \tag{5}$$

where $\langle . \rangle$ and var (.) recall the sample mean (in time) and variance (both in time and space) estimators.

Note that the assumption of stationarity is only reasonable for short temporal intervals (1–1.5 months) and low L values. Since the Caprivi area is observed with S1 data every 12 days, L was set to 3. The neighborhood Ω was then set to a 5×5 spatial window centered on the pixel. The decision to account for a spatial neighborhood in the variance calculation has been determined by the need to decrease the random chance of low $\hat{\nu}$ values that can easily lead to false flood alarms. For the same reason, a lower bound $\nu_{\min}$ on the variance, function of $\hat{\mu}$, has been introduced. This constraint was implemented as

$$\hat{\nu} \longrightarrow \max\left\{\hat{\nu}, \sigma^2_{\min}\right\} \tag{6}$$

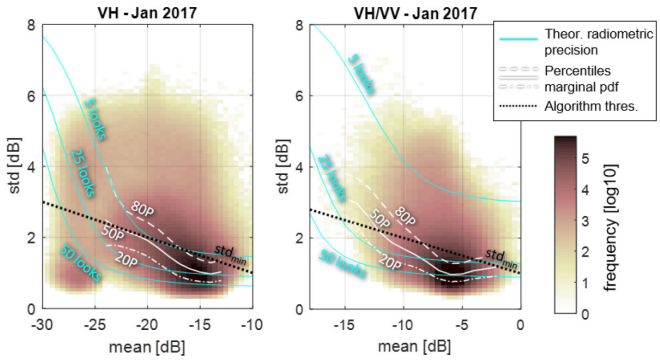

Fig. 6. (Left) Standard deviation of the estimated VH and VH/VV NRCS, $\sqrt{\hat{\nu}_t}$, reported against the associated mean value, $\hat{\mu}_t$. The behavior is shown for the whole floodplain area during a dry acquisition (January 12, 2017) through the bivariate distribution of the model parameters and the 20th, 50th, and 80th percentiles (white lines) calculated on the marginal PDF of $\sqrt{\hat{\nu}_t}$ for every $\hat{\mu}_t$ value. The samples can be related to the theoretical expectations (cyan lines) for fully developed speckle averaged over 5, 25, and 50 looks. The lower bound for the standard deviation of the model [see (6)] is shown in the black-dotted line.

with $\sigma^{[\text{VH}]}_{\min} = -0.1 \cdot \hat{\mu}^{[\text{VH}]}$ for VH, $\sigma^{[\text{VH/VV}]}_{\min} = -0.1 \cdot \hat{\mu}^{[\text{VH/VV}]} + 1$ for VH/VV and where the reference to the time t is left implicit.

In both cases, the bound is determined heuristically and decreases for higher feature (VH or VV) values. For the VH feature, the application of (6) leads, for instance, to a minimum standard deviation of 3.5 and 1 dB for $\hat{\mu}$ values of -25 and -10 dB, respectively. The radiometric stability of weak scatterers, with NRCS closer to the NESZ (reported at -25 dB for S1), is affected by the thermal noise to a larger extent than stronger scatterers. This behavior clearly emerges in Fig. 6, where the distributions of the estimated standard deviation values are shown for the month of January 2017, before the start of the flooding event. At least 60% of the samples, i.e., those ranging within the 20th

and 80th percentile intervals (white lines), are located between the theoretical expectations for a fully developed speckle multilooked on 5 and 50 looks. Such a large span is explained by the presence of both extremely heterogeneous and homogeneous areas (both in space and time) in terms of water content and vegetation structure. The impact of the latter is partly reduced in the polarization ratio. This is clearly conveyed in the (right) VH/VV panel, where the distribution is more skewed toward the 50 looks.

Finally, Fig. 6 shows that the σ_{min} functions (black lines) approximately fall in the 50th and 80th percentile region, hence conveniently assuming low radiometric stability of the NF pixels in favor of a reduction of false flood alarms.

2) F Model: Similar, to the NF case, the F pixels are statistically modeled as

$$y_t \sim \mathcal{N}(\mu_t^F, \nu_t^F). \tag{7}$$

However, the F model is not pixel adaptive. The same set of parameters μ^F and ν^F are adopted for all the pixels. To account for all the pixels classified as F in the previous iteration, the parameters are estimated as

$$\hat{\mu}_t^F = \langle y_{t-1},\ \forall\ F \text{ pixel at } (t-1) \rangle \tag{8}$$

$$\hat{\nu}_t^F = \text{var}\left(y_{t-1},\ \forall\ F \text{ pixel at } (t-1)\right). \tag{9}$$

The same constraint expression in (6) is applied to $\hat{\nu}^F$. Differently from the NF case, however, the threshold σ_{min} is set to a fixed value of 2.5 dB, determined empirically, for both VH and VH/VV. With concern to the initialization of the F model, the signature for VH is extracted from the Zambezi and Chobe River areas. For the VH/VV ratio, the values of $\mu_0^F = -14$ dB and $\nu_0^F = \sigma_{\text{min}}^2$ were instead heuristically chosen. When the image at time $t-1$ does not offer enough F pixels, the last significantly F image or the reference/initialization parameters is used. In this work, the latter option was adopted. In a more refined system, a temporal threshold based on the last F image can be implemented to regulate the selection between the two options.

C. Classification

For every pixel, the algorithm performs at time t one of the following two tests (see Fig. 5), depending on the class label (F or NF) at time $t-1$:

1) NF2F: an NF to F change test if the pixel was classified as NF;
2) F2NF: an F to NF change test if the pixel was classified as F.

The tests are based on the likelihoods computed from the distributions defined in (1) and (7). In the NF2F case, the generalized likelihood ratio test takes the expression

$$\text{LR} = \frac{l_{\text{F}}(t)}{l_{\text{NF}}(t)} = \frac{P(y_t|\mu_t^{\text{F}}, \nu_t^{\text{F}})}{P(y_t|\mu_t, \nu_t)} \underset{\text{NF}}{\overset{\text{F}}{\gtrless}} \gamma \tag{10}$$

where l_{F} and l_{NF} are the two likelihood functions evaluated for the observation y_t.

The change from NF to F conditions is accepted if the probability of the pixel being F is γ times larger than that of being NF, with $\gamma > 1$. A large γ value would yield few false positives (pixels erroneously classified as F) and a large number of false negatives (missed flood pixels). Small values of γ would intuitively lead to the opposite performance outcome.

TABLE II
CLASSES PRODUCED BY FUSING THE VH AND VH/VV MAPS

		VH/VV Map	
		NF	F
VH Map	NF	NF	FV
	F	TW	FV

F—flooded areas; NF—nonflooded areas; TW—temporary open water; FV—flooded vegetation.

For F pixels, the F2NF test is performed, defined as

$$\text{LR} = \frac{l_{\text{NF}}(t)}{l_{\text{F}}(t)} = \frac{P(y_t|\mu_{t_{\text{start}}}, \nu_{t_{\text{start}}})}{P(y_t|\mu_t^F, \nu_t^F)} \underset{\text{F}}{\overset{\text{NF}}{\gtrless}} \beta \tag{11}$$

where $\beta > 1$ regulates the return of the surface to dry conditions and t_{start} refers to the time of the last NF observation of the pixel in the time series. The PDF parameters μ_t and ν_t stop being updated when the pixel is labeled as F. A pixel, therefore, returns to its NF status when its current and preflood backscatter values are almost equal and very different from the overall F area signature.

The outcome from (10) and (11) is spatially processed to remove outliers, by applying a majority filter with a 5×5 window size. The model parameters for the next iteration, at time $t+1$, are calculated by (4), (5), (8), and (9).

D. Flood Map Fusion

The flood mapping process is extended by fusing the VH output with the VH/VV output. In light of the analysis in Section III, the two flood maps can be combined, as shown in Table II, to synthesize the following three LC classes (with their acronyms): NF, FV, and TW.

E. Calibration and Validation

1) Calibration and Cross-Validation With Landsat: The performance of the proposed algorithm was evaluated by comparing the classification results to cloud-free LS8 maps. The use of optical imagery to validate SAR water detection has become a common practice, despite the potential errors in delineating inundated areas using optical data [2], [23], [36]. The LS8 water maps were produced by thresholding the popularly used normalized difference wetness index (NDWI) [37]–[40]. The NDWI highlights the strong absorption of near-infrared (NIR) radiation by water features, contrasting to other water extraction indices, such as the modified normalized difference water index [41], which works better in delineating water and built-up areas in urban areas. The NDWI image can theoretically be segmented using a threshold value of zero. However, differences in geographical image characteristics can create a differing range of values, requiring the need for individual image thresholding. To

achieve this, Otsu's segmentation method, which maximizes the variance between the water and nonwater classes, was used [24]. The NDWI is calculated as follows:

$$\text{NDWI} = \frac{\rho_G - \rho_{\text{NIR}}}{\rho_G + \rho_{\text{NIR}}} \tag{12}$$

where ρ_G is the spectral reflectance in the green (band 2) region of the spectrum and ρ_{NIR} is the spectral reflectance in the NIR (band 5) regions of the spectrum.

The comparison was carried out on the total F area obtained by merging (Boolean union) the FV and TW pixel sets (see Table II, or, equivalently, by merging the F pixels from the VH and VH/VV maps. The user [see (13)] and producer accuracy [see (14)] performance indicators are adopted for the flood class

$$\text{Precision} = \frac{\#(\text{S1 flood AND LS8 flood})}{\#(\text{S1 flood})} \tag{13}$$

$$\text{Recall} = \frac{\#(\text{S1 flood AND LS8 flood})}{\#(\text{LS8 flood})}. \tag{14}$$

The classified data are the S1-based maps and the reference data are the LS8-based maps. Equations (13) and (14) are evaluated by matching the closest LS8 map (in time) to the S1 map under assessment over the region in Fig. 1.

The calibration procedure aims at achieving a convenient tradeoff between precision and recall during the two flood transition phases: the flood expansion phase and the flood recession phase. The precision–recall symmetry (Precision = Recall) is obtained when the F area from S1 equals that from LS8. In this study, the calibration was performed in the 2017 season. First, γ is adjusted by analyzing the algorithm output for the March 25 (flood expansion) and April 6 (flood peak) acquisitions, as illustrated in Fig. 7. The selected threshold, $\gamma = 5$, overestimates the flood extent during its early stages and slightly underestimates it during the peak. Then, the May 12 and June 29 (flood recession phase) acquisitions were used to calibrate β, which regulates the flexibility between F and NF conditions. As conveyed by the right panels in Fig. 7, the selected value, $\beta = 30$, provides a good match for the May 12 acquisitions and a 5-km^2 area excess with respect to LS8 at the end of the flood. The performance is evaluated on all the available S1–LS8 pairs, as shown in Fig. 3, including the aforementioned ones used for calibration. In interpreting the results, the reader shall, hence, consider that a minimal positive performance bias could apply to the latter.

2) Validation With In Situ Data: The flood classification results produced by the algorithm were assessed using the observations collected during the *in situ* surveys. The evaluation was performed on the map generated from the S1 acquisition on April 6, 2017, as it closely matched the *in situ* observations (April 4–7). The same map has been used for the calibration of the algorithm in its expansion phase (threshold γ). Therefore, the S1 results are likely to be affected by a marginal bias in terms of adherence to the LS8 results. Several classification accuracy measures were implemented, namely the producer's accuracy (PA), user's accuracy (UA), overall accuracy (OA), and Kappa (K) [42]. In contrast to (13) and (14), the PA and UA are herewith evaluated on both the NF and F classes (as their

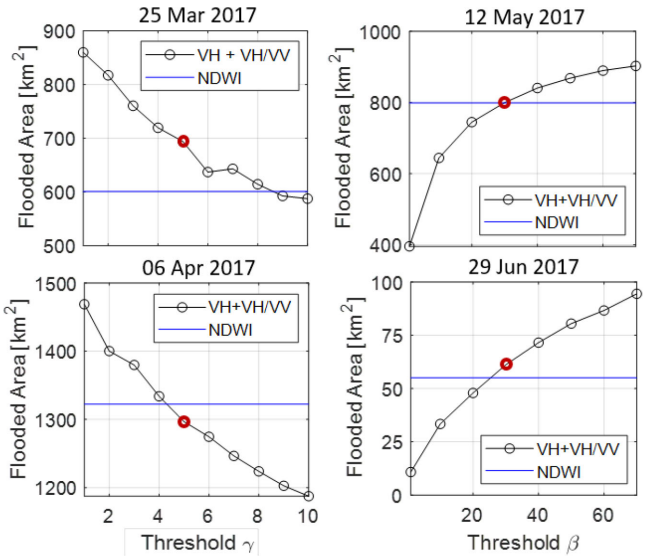

Fig. 7. Algorithm calibration. The total F area (TW + FV) is evaluated for different thresholds γ (left panels) during the flood expansion (March 25, 2017) and flood peak (April 6, 2017), and for different threshold β (right panels) during the flood recession (May 12 and June 29, 2017). The area estimated from the matching LS8 acquisitions by NDWI thresholding is also reported, and the selected thresholds ($\gamma = 5$ and $\beta = 30$) are highlighted.

average). A McNemar's test [43] was also performed to assess the statistical significance of the improvements brought by the map fusion (VH + VH/VV) compared to using a single feature (VH or VH/VV). The test is nonparametric, assuming that the number of correctly and incorrectly identified points is equal for both classifications [44], [45]. Differences were considered as statistically significant at the 5% confidence level, thus, for a Z value greater than 1.96.

V. Results

A. Model Analysis on Exemplary Time Series

This section elaborates on the behavior of the proposed algorithm by focusing on exemplary time series covering the 2017 and 2018 flood events. Two LC features, namely, short grass and tall grass, are used for demonstration purposes. The short grass series refers to a pixel at coordinates Lat, Lon $= -17.5950$, 24.6137, the same represented by the blue line in Fig. 4, whereas the second belongs to a thicker grass field at point coordinates -17.5853, 24.6496. The analysis is supported by the panels in Fig. 8 that illustrate the temporal behavior of the VH, VV, and VH/VV backscatter data. The NF and F model parameters retrieved by the algorithm are presented through the brown- and blue-colored stripes. The LC conditions on April 4–7, 2017 are also conveyed by means of *in situ* pictures.

In the short grass scenario, the VH and VV channels have similar temporal behavior. On the contrary, the VH/VV ratio appears flattened around -8 dB, reaching low values (-13 dB) only during a couple of acquisitions. On both occasions, the drop is, however, too gradual to be recognized as a flood by the algorithm. The flood events, as expected from Section III, are only detected through the sharp VH (8–9 dB) drops in March

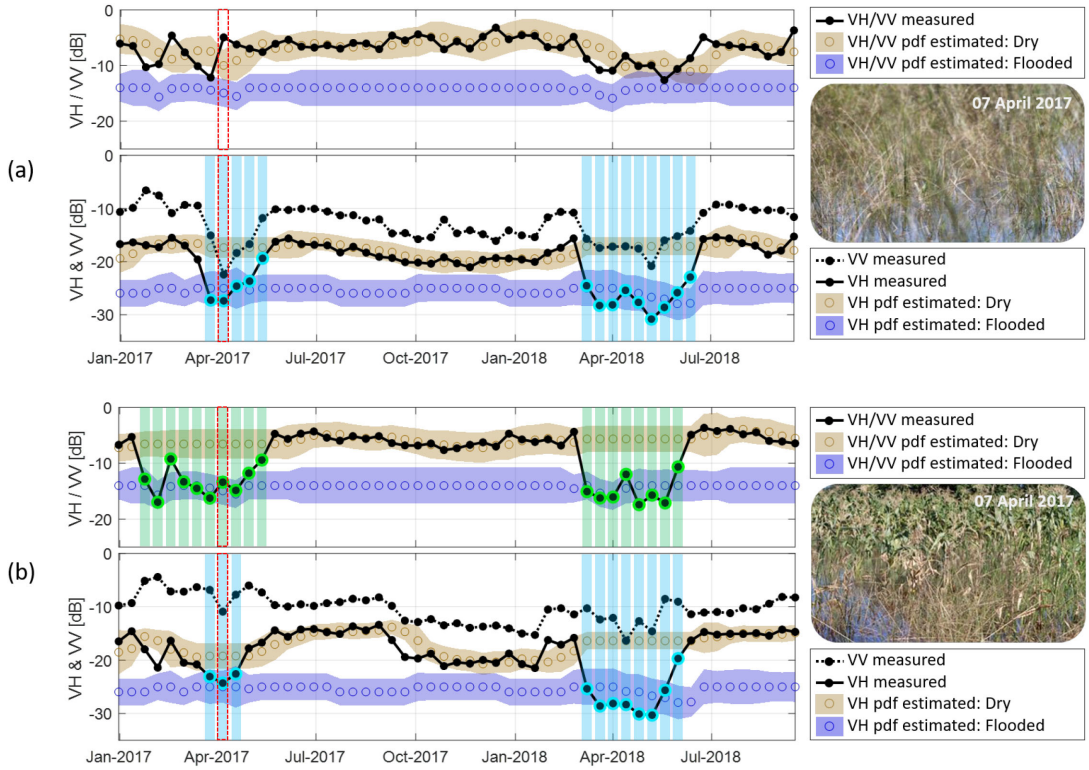

Fig. 8. Example of S1 time series for: (a) a pixel of short grass (<30 cm) at lat,lon = (−17.5950,24.6137); (b) a pixel of tall grass (>30 cm) at lat,lon = (−17.5853, 24.6496). The green and blue vertical bars indicate the F dates as mapped respectively by the VH and VH/VV algorithms. The brown and blue-colored series refer respectively to the PDFs of the dry/NF (brown) and of the F (blue) signatures used for the classification test. Both the mean value (circle markers) and the standard deviation (given by stripe width) of the PDF are represented. The ground campaign dates (April 4–7, 2017) are also highlighted through red dashed boxes.

(for both years). Fig. 8(b) shows the tall grass series. On the contrary, it can be observed that the FV conditions are identified by the VH/VV ratio in both the 2017 and 2018 flood events. It is also interesting to notice that the double-bounce mechanisms associated with FV are significantly stronger in 2017. This can be inferred from the higher VH and VV NRCS values (+6 dB approximately) during the March–April period. In 2018, the double-bounce mechanisms produce a slight VV enhancement as it could barely compensate for the loss of volume scattering. A large drop in VH is observed as a result. This can be as a result of either a higher flood stage reached in 2018 or differences in vegetation phenology between the two years.

From Fig. 8, it can be observed that the model estimates, especially with reference to the dry pixel-adaptive (NF) signatures, follow the data with an apparent delay. This smoothing effect, introduced by the temporal integration window set to a size of $L = 3$ samples, plays a fundamental role in avoiding that the signature to follow the data in abrupt changes. However, some exceptions might arise when a slight VH or VH/VV decrease is encountered during the flood onset, as shown in Fig. 8(b) by the VH/VV ratio behavior during March 2017. In such situations, the dry (NF) signature, μ_t, drifts toward that of the water signature, μ_t^F, with a partial loss in discrimination capabilities of the algorithm. Nevertheless, it can be observed that even in such critical scenarios, the classifier manages to produce a reasonable output.

B. Open Water and FV Maps on the Entire Floodplain

The flood estimates provided by VH, VH/VV, and the fusion of the two products are analyzed over the entire Caprivi floodplain. Fig. 9 shows the results of the spatial evolution of the flood from March 13 to May 12, 2017. The plotted fusion (VH + VH/VV) maps show that the inundation started along the Zambezi River then quickly extending toward the west, close to Chobe River. This region, which is between the two rivers, has the highest vegetation density during the rainy season, and the maps, as expected, exhibit a large FV component (shown in red in Fig. 9). The flood then progresses to the southern portion of the floodplain, which is more sparsely vegetated. At this time, the maps exhibit a predominant TW component (shown in blue in Fig. 9). Overall, the eastern parts of the floodplain experience most of the inundation, and F areas are noticeable for about two months.

Fig. 10 shows the F area extent (km^2) during the 2017 and 2018 flood seasons. S1 provides images throughout the year. SAR data are better for flood monitoring, specifically during floods when the cloud cover is high. In most areas, the area that is F is obscured by clouds, which motivate the use of SAR data. In this regard, the algorithm allows for continuous monitoring throughout both phases of the flood, with a reliable false alarm performance during the dry season (from August to January), as less than 70 km^2 remain labeled as F. Thanks to the regular

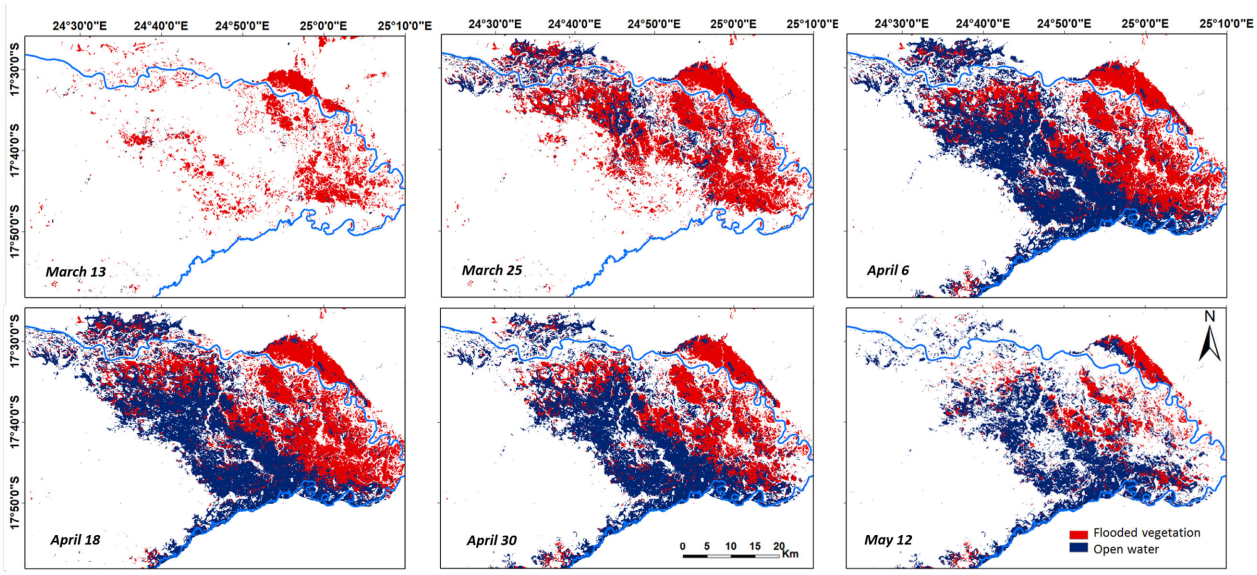

Fig. 9. Fusion of VH and VH/VV flood maps of the Caprivi floodplain from March 13, 2017 to May 12, 2017.

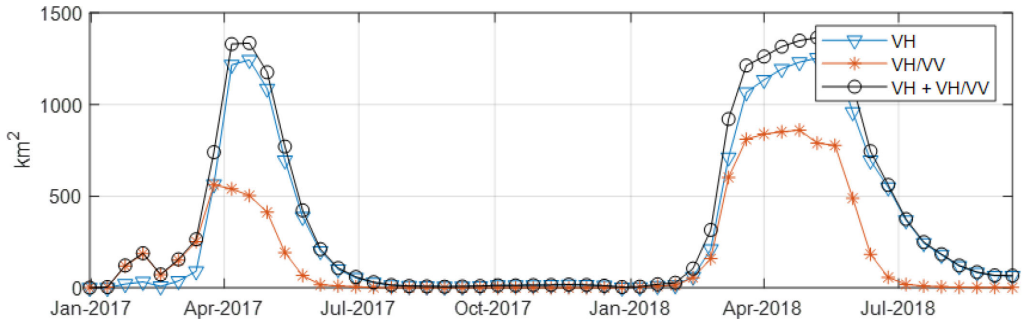

Fig. 10. Multitemporal comparison of the F area extracted from VH, VH/VV, and the union of the two.

revisit of S1, it can be observed that the time to maximum flood extent is very short, unlike the time it takes for the flood to recede. The polarization ratio effectively captures the flood in its initial phase in both seasons. This can be clearly seen for 2017, as the VH contribution is almost null in the first month (until the end of March). In contrast, the VH is more sensitive and complementary (with respect to VH/VV) at the onset of the 2018 flood. These interyear differences are likely due to the fact that the 2018 flood was more severe.

Different plant phenologies during the time of inundation may also have played a role, as shown in Fig. 8. In addition, the differences between the two flood cycles can be seen by comparing the duration of the flood in each season (two months longer in 2018) and the F area returned by the VH/VV ratio (see Fig. 10). Furthermore, the application of the rule in Table II would lead to the observation of a larger FV extent, as identified in 2018. However, closer analysis, aided by Fig. 4, revealed that low VH/VV values were occasionally associated with open water, such as in the case of very low VH (< -28 dB) and VV (< -14 dB) values. This is attributed to a small percentage of TW pixels (typically characterized by very low VH NRCS) within the FV-labeled pixels. Such class confusion is inherent to the simplified definition of FV and is most likely to occur during high flood levels, which partly explains the interyear VH/VV discrepancies between the 2017 and 2018 flood events.

C. Validation Against In Situ Data

The April 6 algorithm output was compared to the LC information collected during the surveying campaign and to the April 10 LS8 flood map. Fig. 11 shows the PA, UA, OA, and K values for the algorithm VH, VH+VH/VV outputs, and for LS8. The PA values for the F class are 84.7%, 96.5%, and 93.4% respective of VH, LS8, and VH + VH/VV images. For each VH + VH/VV image, increasing values of OA and Cohen's Kappa from VH demonstrate the contribution of VH/VV to the accuracy of the SAR-derived flood extent map.

The PA for identifying the water pixels is significantly better for the LS8, displaying less misclassification of nonwater features as water. In general, the OA of LS8 is 8% higher than that of the VH + VH/VV. The Kappa coefficient (K) varies from 0.74 for VH to 0.85 for LS8 showing a good relationship between the

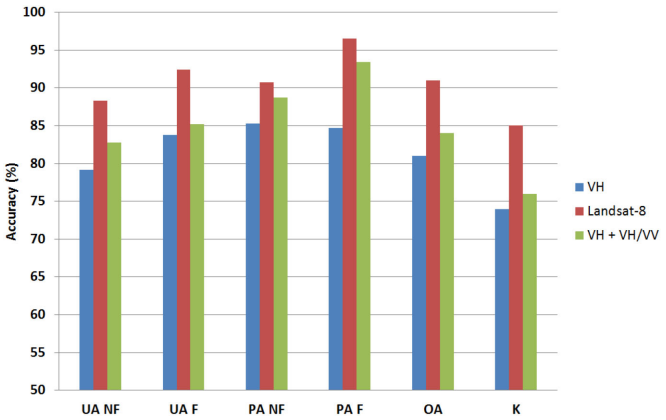

Fig. 11. Overall classification accuracy results for VH, LS8, and fusion of VH + VH/VV. The S1 and LS8 (NDWI) results are based on the April 6 and 10, 2017 acquisitions, respectively.

ground observations result and the satellite data, with minimal correlation caused by chance.

On average, the OA achieved on the classification of the fused dataset is about 5% higher compared to the VH-based classification. McNemar's test showed that the difference in accuracies when the VH and VH+VH/VV datasets were used as input is statistically significant ($Z > 1.96$). Therefore, the study claims that the proposed fusion method has greater potential than using only VH for detecting floods using S1.

D. Comparison With Landsat-8

The comparative analysis with LS8 is approached by addressing the F area extent and the performance metrics in (13) and (14). These are computed for the whole 2017–2018 span, as shown in Fig. 12. The calculation accounts only for the cloud-free areas in the Landsat imagery, whose percentage is reported with a blue line in the top panel (see Fig. 12). The analysis is conducted on the total F area extent, with no distinction between FV and open water. Fig. 12 shows that S1 provides a close match with LS8 throughout both the 2017 and 2018 flood seasons. For 2017, a good match is achieved during the flood peak, with a balanced 87% on precision and recall (it shall be reminded that the amount of S1-only positives match that of LS8-only positives when the estimated F areas are equal), whereas the percentage drops approximately to 75% during the expansion and recession phases. The slight unbalances in favor of precision during the flood expansion phase are in agreement with the calibration choices in Fig. 7. The performance behavior during 2018 is qualitatively comparable to that of 2017, despite the differences in the timing and the extent of the two flood events. The maximum joint agreement of 85% is registered in the second half of May 2018 close to the flood expansion peak. The similarity is slightly poorer (<80%) and more unbalanced during the other flood phases, with S1 more than LS8 before the peak and less sensitive during the recession phase.

A visual inspection of the matching and nonmatching features in two locations, one along the Zambezi and one along the Chobe river (labeled as region of interest in Fig. 1), was carried out, supported by Fig. 13 to better understand the differences in accuracies between the LS8 and S1 products. In the Zambezi region, the attention is drawn, at first, to the area adjacent to the river, contoured by a dashed yellow line. The S1 algorithm underestimated the F area both before (March 25, 2017) and after (May 12, 2017) the flood peak. This behavior is mainly attributed to the poor resolution of the S1 maps when compared to scale of the LC heterogeneity in the river proximity, consisting of narrow grass patches and higher vegetation (shrubs and trees). The resolution of S1 maps is reduced with respect to the nominal S1 GRD pixel after the speckle and the majority filtering steps in the preprocessing and postprocessing, respectively. As a result, LS8 has a higher effective resolution, but this is partly compensated by a higher sensitivity of the S1 product in open grass areas.

During the flood recession phase, the S1 map reported more F areas than LS8. Still within the Zambezi region, and especially in the area contoured by a cyan dashed line (see Fig. 13), the S1 positives (F for S1 and NF for LS8) are mainly attributable to the polarization ratio, as the VH present insignificant anomalies. The same behavior is observed in the Chobe region during the 2017 flood expansion (March 25). Apparent double-bounce reflections can be observed especially in the northwestern area (as evident from the VV NRCS enhancement). In the same location, the NDWI shows very low values (< -0.2). These examples clearly illustrate the added value of SAR with respect to the optical indexes, although such benefits only apply to a small percentage of the overall area. The last location marked in Fig. 13 (fourth column) is characterized by a borderline behavior of the radar and optical signatures during the flood recession phase, leading to a missed flood detection from S1. It can be observed that the NDWI and the VH NRCS images present similar spatial heterogeneity, although neither exhibits clear flood anomalies. The discrepancy is then mainly accountable to the choice of the threshold β.

Further insight on the algorithm sensitivity is obtained by investigating the histograms of the optical and radar features for the matching and nonmatching flood map areas on the entire floodplain, shown in Fig. 14. The analysis covers two dates each year. Fortunately, three of these dates have available concurrent LS8 and S1 products. The other matching dates considered are March 12 and March 8, 2018 for LS8 and S1 products respectively. From the NDWI panels, it can be noticed that the S1 negatives and positives (yellow and cyan bell curves, respectively) are skewed toward the NDWI threshold, implying a substantial similarity in the response to the flood between the two sensors, as well as a high sensitivity of the maps to small threshold adjustments. This can also be inferred by analyzing the VH panels. Although the pixel-adaptive threshold makes the plots readability less straightforward, it can be observed that the discrepancies occur for pixels with high VH NRCS when compared to that of the matching pixels (red bell curves). However, such consideration does not apply to the March12, 2018 graph, since the LS8–S1 confusion for this latter is most likely related to the four-day intermap difference.

The most appealing histograms are, however, provided by the VV NRCS and by the VH/VV ratio. The S1 positives and negatives show distinct distributions in these features' domains. The

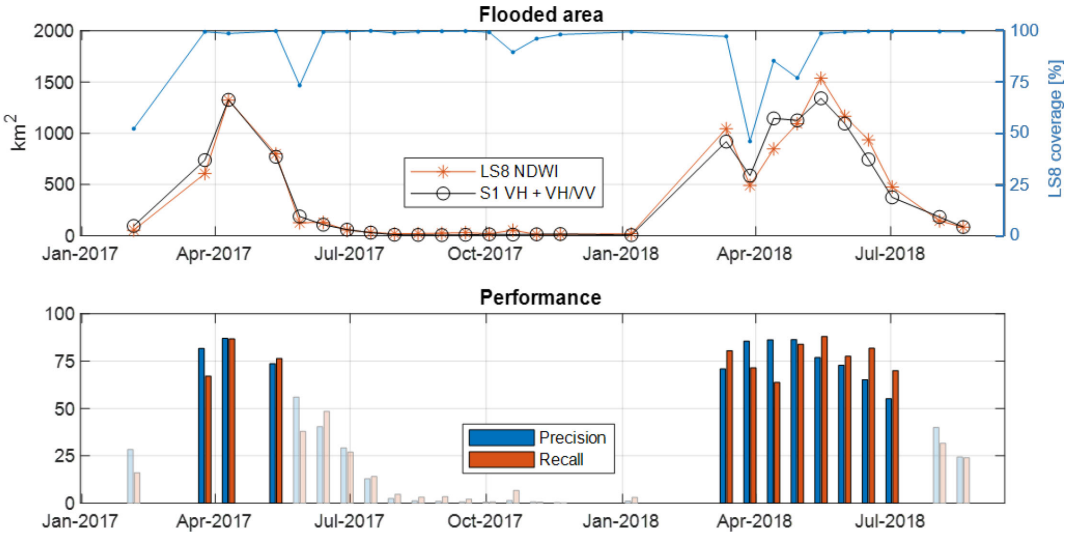

Fig. 12. (Top) Total flood area extent extracted from the Landsat NDWI products and from closest (in date) S1 output (TW + FV). The percentage of cloud-free area in the LS8 imagery is reported in a blue line. Notice that only the unobstructed area is used for the comparison. (Bottom) Precision and recall metrics are reported with saturated colors for the relevant dates and with desaturated colors for images with marginal F area extent.

panels convey that S1 positives can be mainly associated with FV, which are characterized by low ratio and high VV values as a result of double bounce. In contrast, the S1 negatives can be associated with canopy scattering without water–plant enhancements as they occupy a higher VH/VV ratio band indicatively VH/VV > -8 dB. This interpretation is also confirmed by the normalized difference vegetation index (NDVI) panels, where both errors occur at high greenness values, approximately NDVI > 0.5, and thus for substantially developed vegetation. Some interesting NDVI differences are further registered between the 2017 and 2018 events. In 2018, the error distributions are more separated, with distinctively higher NDVI values for S1 positives. This is most likely due to the larger extent and duration of the flood in 2018, which enhances the sensitivity of optical sensors to taller grasses.

Finally, the bimodal behavior of histograms in 2018, especially concerning the matching pixel distributions, is addressed. Such distributions suggest that two different groups of F pixels are present: one is characterized by open water and very low VH and VV NRCS and the second is most likely comprising emerging or floating vegetation, with slightly higher backscatter intensities. However, the first scenario is less pronounced in 2017 due to the lower flood level.

VI. Discussion

The principal objective of this study was to assess the suitability of dual polarized S1 acquisitions (VH + VV) with a short revisit time (twelve days in Africa) for monitoring flood events in a vegetated floodplain. To achieve this aim, the study introduces a novel methodology that makes use of an S1 time series throughout the entire flood event with temporal continuity between different seasons. The model is pixel adaptive, implying that the thresholds for the identification of changes are pixel and time dependent. In particular, the dry (NF) signature of each pixel is retrieved from its NF samples in the previous month (three samples in the 12-day S1 revisit configuration), avoiding, therefore, specific training for different LC types.

The calibration phase of the algorithm consists of the retrieval of two coefficients for the whole scene and the thresholds for the two likelihood ratio tests. The first regulates the transitions from a dry to F land and the second addresses the transition back to dry land. In this study, the coefficients were adjusted by using LS8-derived maps as reference. This makes sense when S1 is used as a gap-filling alternative to optical sensors. In addition, the water signatures for each of the processed VH and VH/VV ratio radar features must be initialized. These signatures are unique for the whole floodplain, although they are allowed to change over time according to (8) and (9). The adoption of a whole-scene signature for F pixels was favored over a pixel-adaptive approach due to the interseasonal variability in flood levels and, hence, in signature responses, which could hinder the flood detection test if poorly addressed. On the other hand, a pixel-adaptive model is deemed potentially beneficial from the F to NF test and, therefore, worthy of further investigation. Note, in addition, that use of whole-scene water parameters facilitates the ease of use and the applicability of the technique to different regions without retraining as their interscenario variability is expected to be low. However, this must be properly assessed in future work, especially in areas with a different LC or illuminated with different (shorter) revisit times than the 12 days available for Caprivi.

The proposed model and the algorithm implementation are conceptually based on two assumptions: 1) large sudden drops in the time series of the VH NRCS or of the VH/VV ratio can be linked to a flood event. The significance of the drop is evaluated by relating it to the preflood mean value and standard deviation; and 2) when returning to NF conditions, the backscatter approaches its preflood levels. These assumptions shaped the methodology in a change detection approach and are, hence,

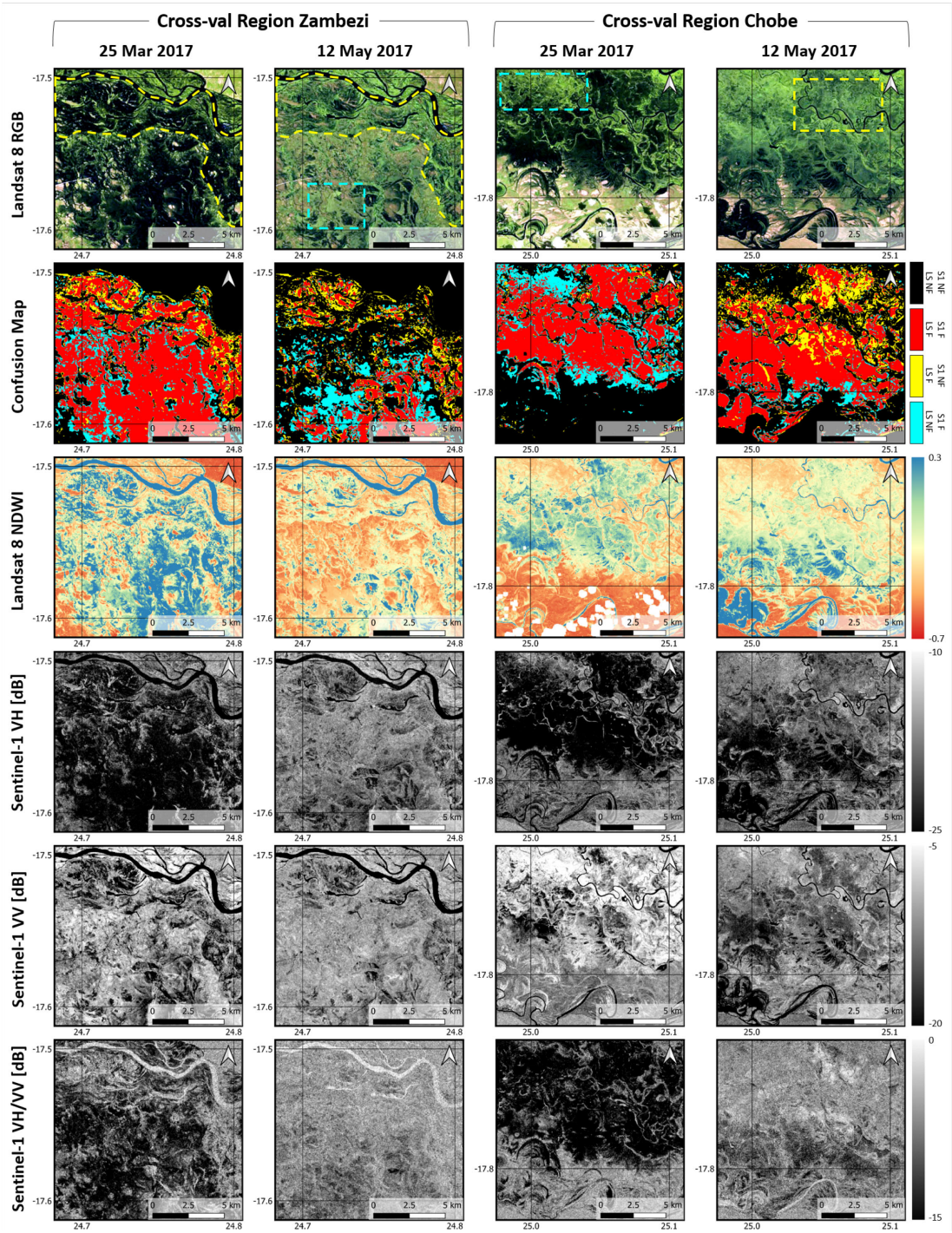

Fig. 13. Flood maps and spectral features/indexes derived from S1 and LS8. The comparison covers the two cross-validation regions shown in Fig. 1. From top to bottom, the panels report the following information: an LS8 RGB color composite (3, 2, 1); an S1–LS8 confusion map showing the matching pixels in red, the S1-only F pixels in cyan, and the LS8-only F pixels in yellow; the LS8 NDWI; the VH NRCS; the VV NRCS; and the VH/VV ratio from S1. The areas characterized by relevant LS8–S1 discrepancies (and therefore commented in Section V-D) are contoured in the upper panels with lines colored in accordance with the associated mismatch.

inherently robust to the well-known confusion problem with persistently low backscatter areas, such as bare dry soil [6], [46]. The devised signature calculation procedures effectively account for the stronger temporal fluctuations typically occurring in such areas, mainly due to NESZ and changes in moisture. It should be noted that both assumptions can expose the algorithm to the risk of false flood positives. In the case of the first assumption, the false positives would be caused by unforeseen and hence unmodeled events (such as deforestation and crop harvest events in agriculture areas). The occurrence of such events can be addressed by introducing additional information, such as interferometric coherence [47], in a postprocessing step or by

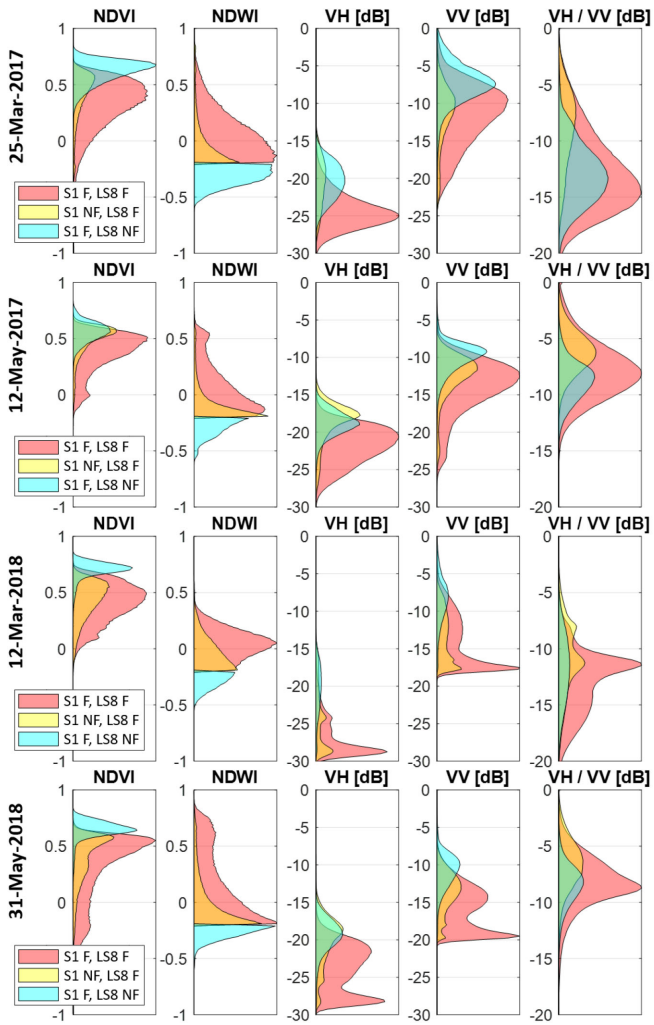

Fig. 14. Analysis of a mismatch between S1 and LS8 flood maps for four representative dates in 2017 and 2018. The panels illustrate the histograms of NDVI and NDWI (LS8) and of VH, VV, and VH/VH (S1) for the matching F pixels (red), for the S1-only F pixels (cyan), and for the LS8-only F pixels (yellow) over the entire floodplain. Note that the March 12, 2018 LS8 product date has been compared with the March 8, 2018 S1 product. Part of the discrepancies can be, hence, attributed to the four-day differences.

removing areas prone to such activities. The second assumption can hinder the return to NF conditions. When the backscatter intensity, with the main reference to the VH NRCS, remains low, the pixel would be labeled as F throughout the dry season. In its current form, the algorithm does not include mechanisms to control such scenarios. In semiarid and rural regions without intense land use, these issues are unlikely to frequently emerge, as conveyed by the results in our study area.

The effectiveness of the proposed method and the sensitivity of the S1 imagery were evaluated by comparing the results to flood maps derived from the LS8 NDWI. As the sensors exhibit similar performances in mapping temporary open water, the sensitivity to FV raised most of the interest. In presence of emerging and floating vegetation, water surface smoothness and high permeability can produce water–plant double bouncing effects, which enhance the backscatter, in particular from the copolarized (VV and HH) channels [3], [7], [23]. Good sensitivity of VH to FV was observed in [23] and [48]. However, other studies, such as [49] and [50], argued that VV polarization is more suited for identifying partially submerged vegetation. Currently, it is well known that single polarizations are unable to properly address the scattering complexity of FV. The use of multiple polarization channels and polarimetric combinations (differences and ratios most notably) has recently been proposed to handle FV [8], [51].

Our study consolidated that the use of both VH and VV polarizations in the form of their ratio (VH/VV) was found to be a convenient strategy to account for the double-bounce effect from FV and provided a phenomenological justification for it. It was observed that the FV in the presence of double-bounce effects spans a wide range of VH and VV values (from -15 to -5 dB for VV and from -30 to -20 dB for VH), as the NRCS depends on both the structure of the canopy and the flood depth, which concurs with previous studies [52]. It was shown (see Fig. 8) that the VV NRCS does not necessarily exhibit an increase with respect to its preflood level.

The overall classification accuracy obtained from the fused VH and VH/VV maps is only slightly inferior to that obtained using the cloud-free LS8, based on the collected *in situ* observations. The use of a single polarization (VH) resulted in a performance loss of up to 5% with respect to the dual-polarized approach, as a significant portion of the FV would be disregarded. The estimated flood extent during the flood peak is very similar to the NDWI-based map with an 85–87% precision and recall performance for both the 2017 and 2018 flood events. The similarity during the expansion and recession phases of the flood registered slightly lower values, which is due to the different responses of the sensors to the vegetation dynamics combined with the adopted calibration strategy (which favored the flood extent matching during the peak).

The discrepancies between the S1 and LS8 flood maps mainly occurred in vegetated areas. In particular, it was observed that the S1 commissions (compared to LS8) correspond to areas with very high values of NDVI (>0.5), whereas the S1 omissions (compared to LS8) can be related to areas with low canopy greenness ($0.3 < \text{NDVI} < 0.6$). The latter also includes F features with pixel size comparable to or lower than that of the resolution of S1 maps, which is hampered by 5×5 majority filter applied in postprocessing. The study, hence, confirmed that polarimetric C-band radar signals are particularly sensitive to partially submerged canopies with vertically oriented elements such as stems and trunks as they lead to double-bounce mechanisms [7], [53], [54]. In contrast, NDWI is more influenced by the amount of open water and the moisture content of the vegetation recorded in a pixel [55].

Despite the relatively long (12-day) revisit time of S1, the ability of SAR to acquire images during cloud cover gives the statistical modeling developed in this study an advantage over methods that make use of optical data. The proposed SAR-based multitemporal technique is suitable for flood monitoring during cloud cover conditions. Application of this method to datasets with shorter revisits intervals is expected to further improve the temporal as well as the spatial delineation of F areas, possibly

bridging the absolute performance gap with optical sensors (under clear-sky conditions). The study also supports evidence of the value VH and VH/VV fusion and demonstrates that the ratio is a convenient way for characterizing the F area in terms of FV and TW. The F areas detected by VH/VV are labeled as FV, whereas the ones revealed exclusively by VH are regarded as TW. The accuracy of such classification procedure has not been thoroughly evaluated as it was out of the scope of this work to associate the labels to a precise LC taxonomy. It was discussed how borderline cases of temporary open water detected by VH/VV (e.g., for Bragg scattering from water) and FV detected by VH cannot be excluded.

In conclusion, the developed method was tested over an area with flat terrain. It is likely that the inclusion of ancillary data (e.g., DEMs that can provide a representation of the floodplain geometry and initial conditions) will improve the performance of the technique in areas with varied topography. However, DEM errors, resolution, or degree of generalization must be carefully considered in the workflow.

VII. Conclusion

This study evaluated the potential of S1 SAR images for the continuous mapping of floodplains dominated by herbaceous vegetation cover. In particular, the work focused on the Caprivi floodplain region and covered the 2017 and 2018 flood events. A novel pixel-based mapping strategy relying on the causal modeling of the VH and VH/VV time series and on two likelihood ratio tests (for the detection of flood start and flood end) is proposed. The method was designed for NRT applications, as the model parameters are retrieved from the past samples in the series. It was shown that the 12-day S1 dataset is capable of adequately delineating the extent of the inundated areas during both the expansion and the recession phases of the flood. The maps produced by the algorithm reach an 85% spatial agreement with the available LS8-derived maps during the period of maximum flood expansion. The agreement was weaker before and after the peak, mainly due to different sensitivity to the FV of the two sensors.

Dual-polarized SAR detected FV when water–plant double-bounce mechanisms occurred. However, it is less sensitive when the plant structure does not generate backscatter enhancements, such as for shorter vegetation. The most significant discrepancies between the S1 and LS8 products were registered during the recession phase, with the agreement dropping to 75%. It was shown that the VH/VV ratio is suited for mapping FV. The *in situ* data, collected during the 2017 event peak, confirmed that the addition of the VH/VV ratio to the VH NRCS leads to a significant increase in absolute accuracy.

Acknowledgment

The authors would like to thank the Namibian Meteorological Department for providing rainfall data and Stellenbosch University Graduate School and TU Delft University for the additional funding.

References

[1] G. Zhao, B. Pang, Z. Xu, J. Yue, and T. Tu, "Mapping flood susceptibility in mountainous areas on a national scale in China," *Sci. Total Environ.*, vol. 615, pp. 1133–1142, 2018.

[2] S. Hong, H. Jang, N. Kim, and H.-G. Sohn, "Water area extraction using RADARSAT SAR imagery combined with landsat imagery and terrain information," *Sensors*, vol. 15, no. 3, pp. 6652–6667, 2015.

[3] A. Twele, W. Cao, S. Plank, and S. Martinis, "Sentinel-1-based flood mapping: A fully automated processing chain," *Int. J. Remote Sens.*, vol. 37, no. 13, pp. 2990–3004, 2016.

[4] P. A. Townsend, "Mapping seasonal flooding in forested wetlands using multi-temporal radarsat SAR," *Photogrammetric Eng. Remote Sens.*, vol. 67, no. 7, pp. 857–864, 2001.

[5] T. D. Acharya, D. H. Lee, I. T. Yang, and J. K. Lee, "Identification of water bodies in a Landsat 8 OLI image using a J48 decision tree," *Sensors*, vol. 16, no. 7, 2016, Art. no. 1075.

[6] S. Martinis, S. Plank, and K. Ćwik, "The use of Sentinel-1 time-series data to improve flood monitoring in arid areas," *Remote Sens.*, vol. 10, no. 4, 2018, Art. no. 583.

[7] S. Plank, M. Jüssi, S. Martinis, and A. Twele, "Mapping of flooded vegetation by means of polarimetric Sentinel-1 and ALOS-2/PALSAR-2 imagery," *Int. J. Remote Sens.*, vol. 38, no. 13, pp. 3831–3850, 2017.

[8] V. Tsyganskaya, S. Martinis, P. Marzahn, and R. Ludwig, "SAR-based detection of flooded vegetation—A review of characteristics and approaches," *Int. J. Remote Sens.*, vol. 39, no. 8, pp. 2255–2293, 2018.

[9] L. White, B. Brisco, M. Pregitzer, B. Tedford, and L. Boychuk, "RADARSAT-2 beam mode selection for surface water and flooded vegetation mapping," *Can. J. Remote Sens.*, vol. 40, no. 2, pp. 135–151, 2014.

[10] C. Kuenzer, H. Guo, J. Huth, P. Leinenkugel, X. Li, and S. Dech, "Flood mapping and flood dynamics of the mekong delta: ENVISAT-ASAR-WSM based time series analysis," *Remote Sens.*, vol. 5, no. 2, pp. 687–715, 2013.

[11] S. Schlaffer, P. Matgen, M. Hollaus, and W. Wagner, "Flood detection from multi-temporal SAR data using harmonic analysis and change detection," *Int. J. Appl. Earth Observ. Geoinf.*, vol. 38, pp. 15–24, 2015.

[12] L. Giustarini *et al.*, "Probabilistic flood mapping using synthetic aperture radar data," *IEEE Trans. Geosci. Remote Sens.*, vol. 54, no. 12, pp. 6958–6969, Dec. 2016.

[13] F. Bioresita, A. Puissant, A. Stumpf, and J. P. Malet, "A method for automatic and rapid mapping of water surfaces from Sentinel-1 imagery," *Remote Sens.*, vol. 10, no. 2, 2018, Art. no. 217.

[14] S. Grimaldi, J. Xu, Y. Li, V. R. N. Pauwels, and J. P. Walker, "Flood mapping under vegetation using single SAR acquisitions," *Remote Sens. Environ.*, vol. 237, 2020, Art. no. 111582.

[15] H. S. Srivastava, P. Patel, Y. Sharma, and R. R. Navalgund, "Multi-frequency and multi-polarized SAR response to thin vegetation and scattered trees," *Current Sci.*, vol. 97, no. 3, pp. 425–429, 2009.

[16] C. Cazals *et al.*, "Mapping and characterization of hydrological dynamics in a coastal marsh using high temporal resolution Sentinel-1A images," *Remote Sens.*, vol. 8, no. 7, 2016, Art. no. 570.

[17] M. Mleczko and M. Mróz, "Wetland mapping using SAR data from the Sentinel-1A and tanDEM-X missions: A comparative study in the Biebrza floodplain (Poland)," *Remote Sens.*, vol. 10, no. 1, 2018, Art. no. 78.

[18] J. Muro *et al.*, "Short-term change detection in wetlands using Sentinel-1 time series," *Remote Sens.*, vol. 8, no. 10, 2016, Art. no. 795.

[19] L. Pulvirenti, N. Pierdicca, M. Chini, and L. Guerriero, "Monitoring flood evolution in vegetated areas using COSMO-skymed data: The Tuscany 2009 case study," *IEEE J. Sel. Topics Appl. Earth Observ. Remote Sens.*, vol. 6, no. 4, pp. 1807–1816, Aug. 2013.

[20] S. Martinis, A. Twele, and S. Voigt, "Towards operational near real-time (NRT) flood detection using a split-based automatic thresholding procedure on high resolution terraSAR-X data," *Natural Hazards Earth Syst. Sci.*, vol. 9, no. 2, pp. 303–314, 2009.

[21] P. Matgen, R. Hostache, G. Schumann, L. Pfister, L. Hoffmann, and H. Savenije, "Towards an automated SAR-based flood monitoring system: Lessons learned from two case studies," *Phys. Chem. Earth, A/B/C*, vol. 36, no. 7, pp. 241–252, 2011.

[22] V. Tsyganskaya, S. Martinis, and P. Marzahn, "Flood monitoring in vegetated areas using multitemporal Sentinel-1 data: Impact of time series features," *Water*, vol. 11, no. 9, 2019, Art. no. 1938.

[23] V. Tsyganskaya, S. Martinis, P. Marzahn, and R. Ludwig, "Detection of temporary flooded vegetation using Sentinel-1 time series data," *Remote Sens.*, vol. 10, no. 8, 2018, Art. no. 1286.

[24] N. Otsu, "A threshold selection method from gray-level histograms," *Automatica*, vol. 11, nos. 285–296, pp. 23–27, 1975.
[25] J. Mendelsohn, C. Robets, and C. Hines, *An Environmental Profile and Atlas of Caprivi*. Windhoek, Namibia: Directorate of Environmental Affairs, 1997.
[26] S. Long, E. Fatoyinbo, Temilola, and F. Policelli, "Flood extent mapping for Namibia using change detection and thresholding with SAR," *Environ. Res. Lett.*, vol. 9, no. 3, 2014, Art. no. 035002.
[27] S. Skakun, N. Kussul, A. Shelestov, and O. Kussul, "Flood hazard and flood risk assessment using a time series of satellite images: A case study in Namibia," *Risk Anal.*, vol. 34, no. 8, pp. 1521–1537, 2014.
[28] B. Van der Waal, "Aspects of the fishery of the eastern Caprivi, Namibia," *Madoqua*, vol. 17, no. 1, pp. 1–16, 1990.
[29] S. Martinis, "Improving flood mapping in arid areas using sentinel-1 time series data," in *Proc. IEEE Int. Conf. Geosci. Remote Sens. Symp.*, Fort Worth, TX, USA, 2017, pp. 193–196.
[30] B. Pradhan, M. I. Sameen, and B. Kalantar, "Optimized rule-based flood mapping technique using multitemporal RADARSAT-2 images in the tropical region," *IEEE J. Sel. Topics Appl. Earth Observ. Remote Sens.*, vol. 10, no. 7, pp. 3190–3199, Jul. 2017.
[31] P. A. Hwang, B. Zhang, J. V. Toporkov, and W. Perrie, "Comparison of composite Bragg theory and quad-polarization radar backscatter from RADARSAT-2: With applications to wave breaking and high wind retrieval," *J. Geophys. Res.: Oceans*, vol. 115, no. C11, 2010.
[32] H. Shen, W. Perrie, Y. He, and G. Liu, "Wind speed retrieval from VH dual-polarization RADARSAT-2 SAR images," *IEEE Trans. Geosci. Remote Sens.*, vol. 52, no. 9, pp. 5820–5826, Sep. 2014.
[33] J. Park, J. Won, A. A. Korosov, M. Babiker, and N. Miranda, "Textural noise correction for sentinel-1 TOPSAR cross-polarization channel images," *IEEE Trans. Geosci. Remote Sens.*, vol. 57, no. 6, pp. 4040–4049, Jun. 2019.
[34] D. Eilander, F. O. Annor, L. Iannini, and N. Van de Giesen, "Remotely sensed monitoring of small reservoir dynamics: A Bayesian approach," *Remote Sens.*, vol. 6, no. 2, pp. 1191–1210, 2014.
[35] J.-S. Lee, J.-H. Wen, T. L. Ainsworth, K.-S. Chen, and A. J. Chen, "Improved sigma filter for speckle filtering of SAR imagery," *IEEE Trans. Geosci. Remote Sens.*, vol. 47, no. 1, pp. 202–213, Jan. 2009.
[36] A. Amazirh *et al.*, "Retrieving surface soil moisture at high spatio-temporal resolution from a synergy between sentinel-1 radar and landsat thermal data: A study case over bare soil," *Remote Sens. Environ.*, vol. 211, pp. 321–337, 2018.
[37] S. K. McFeeters, "The use of the normalized difference water index (NDWI) in the delineation of open water features," *Int. J. Remote Sens.*, vol. 17, no. 7, pp. 1425–1432, 1996.
[38] T. Bangira, S. Alfieri, M. Menenti, A. van Niekerk, and Z. Vekerdy, "A spectral unmixing method with ensemble estimation of endmembers: Application to flood mapping in the caprivi floodplain," *Remote Sens.*, vol. 9, no. 10, 2017, Art. no. 1013.
[39] A. Goffi, D. Stroppiana, P. A. Brivio, G. Bordogna, and M. Boschetti, "Towards an automated approach to map flooded areas from sentinel-2 MSI data and soft integration of water spectral features," *Int. J. Appl. Earth Observ. Geoinf.*, vol. 84, 2020, Art. no. 101951.
[40] X. Huang, C. Wang, and Z. Li, "A near real-time flood-mapping approach by integrating social media and post-event satellite imagery," *Ann. GIS*, vol. 24, no. 2, pp. 113–123, 2018.
[41] Y. Du, Y. Zhang, F. Ling, Q. Wang, W. Li, and X. Li, "Water bodies' mapping from sentinel-2 imagery with modified normalized difference water index at 10-m spatial resolution produced by sharpening the SWIR band," *Remote Sens.*, vol. 8, no. 4, 2016, Art. no. 354.
[42] G. M. Foody, "Thematic map comparison: Evaluating the statistical significance of differences in classification accuracy," *Photogrammetric Eng. Remote Sens.*, vol. 70, no. 5, pp. 627–633, 2004.
[43] Y. Lu, M. Wang, and G. Zhang, "A new revised version of McNemar's test for paired binary data," *Commun. Statist. - Theory Methods*, vol. 46, pp. 10010–10024, 2017.
[44] T. Kavzoglu and I. Colkesen, "An assessment of the effectiveness of a rotation forest ensemble for land-use and land-cover mapping," *Int. J. Remote Sens.*, vol. 34, no. 12, pp. 4224–4241, 2013.
[45] J. de Leeuw, H. Jia, L. Yang, X. Liu, K. Schmidt, and A. K. Skidmore, "Comparing accuracy assessments to infer superiority of image classification methods," *Int. J. Remote Sens.*, vol. 27, no. 1, pp. 223–232, 2006.
[46] D. O'Grady, M. Leblanc, and D. Gillieson, "Use of ENVISAT ASAR global monitoring mode to complement optical data in the mapping of rapid broad-scale flooding in Pakistan," *Hydrol. Earth Syst. Sci.*, vol. 15, pp. 3475–3494, 2011.
[47] L. Pulvirenti, M. Chini, N. Pierdicca, and G. Boni, "Use of SAR data for detecting floodwater in urban and agricultural areas: The role of the interferometric coherence," *IEEE Trans. Geosci. Remote Sens.*, vol. 54, no. 3, pp. 1532–1544, Mar. 2016.
[48] T. Westra, R. D. Wulf, F. V. Coillie, and S. Crabbe, "Optimal Envisat advanced synthetic aperture radar image parameters for mapping and monitoring Sahelian floodplains," *J. Appl. Remote Sens.*, vol. 4, no. 1, 2010, Art. no. 043511.
[49] P. Manjusree, L. Prasanna Kumar, C. M. Bhatt, G. S. Rao, and V. Bhanumurthy, "Optimization of threshold ranges for rapid flood inundation mapping by evaluating backscatter profiles of high incidence angle SAR images," *Int. J. Disaster Risk Sci.*, vol. 3, no. 2, pp. 113–122, 2012.
[50] M. A. Clement, C. G. Kilsby, and P. Moore, "Multi-temporal synthetic aperture radar flood mapping using change detection," *J. Flood Risk Manage.*, vol. 11, pp. 152–168, 2018.
[51] B. Brisco, M. Kapfer, T. Hirose, B. Tedford, and J. Liu, "Evaluation of C-band polarization diversity and polarimetry for wetland mapping," *Can. J. Remote Sens.*, vol. 37, no. 1, pp. 82–92, 2011.
[52] L. Pulvirenti, M. Chini, N. Pierdicca, L. Guerriero, and P. Ferrazzoli, "Flood monitoring using multi-temporal COSMO-skymed data: Image segmentation and signature interpretation," *Remote Sens. Environ.*, vol. 115, no. 4, pp. 990–1002, 2011.
[53] S. Mahdavi, B. Salehi, J. Granger, M. Amani, B. Brisco, and W. Huang, "Remote sensing for wetland classification: A comprehensive review," *GISci. Remote Sens.*, vol. 55, no. 5, pp. 623–658, 2018.
[54] M. Mahdianpari, B. Salehi, F. Mohammadimanesh, and M. Motagh, "Random forest wetland classification using ALOS-2 l-band, RADARSAT-2 c-band, and terraSAR-X imagery," *ISPRS J. Photogrammetry Remote Sens.*, vol. 130, pp. 13–31, 2017.
[55] M. Boschetti, F. Nutini, G. Manfron, P. A. Brivio, and A. Nelson, "Comparative analysis of normalised difference spectral indices derived from MODIS for detecting surface water in flooded rice cropping systems," *PloS one*, vol. 9, no. 2, 2014, Art. no. 0088741.

Tsitsi Bangira received the M.Sc. degree in geo-information sciences and remote sensing specializing in water resources and environmental management from the University of Twente, Enschede, The Netherlands, in 2013, and the Ph.D. degree in Geography and Environmental Studies from the University of Stellenbosch, Stellenbosch, South Africa.

Her main research interests include surface water mapping, particularly in heterogeneous environments using optical and synthetic aperture radar data.

Lorenzo Iannini received the master's degree in telecommunications engineering and the Doctoral degree in the polarimetric calibration of synthetic aperture radars (SARs) from the Politecnico di Milano, Milan, Italy, in 2008 and 2013, respectively.

Since 2012, he has been with the Department of Geoscience and Remote Sensing, Delft University of Technology, Delft, The Netherlands. During the ten-year experience with the Politecnico di Milano and the Delft University of Technology, he was involved in multiple project initiatives aimed at devising radar processing algorithms for land cover monitoring and evaluating SAR systems performance, including the participation in European Space Agency feasibility study phases. His current research interests include system design and performance assessment of multistatic SAR system formations and the integration of radar and optical satellite data for the timely mapping of land cover.

Massimo Menenti is an internationally renowned scientist in the fields of Earth observation and global terrestrial water cycle . He is currently with the Delft University of Technology, Delft, The Netherlands. His outstanding achievements have been attained in the aspects of surface parameter retrievals from remote sensing, remote sensing-based evapotranspiration (ET) estimation, time-series analysis of remote sensing products, and the application of remote sensing technology in hydrology and climate models. He is one of the earliest researchers in using laser radar technology to measure surface aerodynamic roughness. He initiated the use of time series analysis techniques to extract information from satellite data. He presented the surface energy balance index (SEBI) theory for ET estimation, which is the prototype of the following S-SEBI, SEBS, and SEBAL models. He held senior researcher positions in The Netherlands, France, the USA, and Italy and has coordinated many large European projects with participants from Europe, Asia, America, and Africa.

Adriaan van Niekerk received the Ph.D. degree in Geography and Environmental Studies from Stellenbosch University, Stellenbosch, South Africa.

He is currently an Associate Professor with Stellenbosch University. His research interests include application and development of geographical information systems and remote sensing (earth observation) techniques to support decisions concerned with land use, biogeographical, environmental, and socioeconomic problems.

Zoltan Vekerdy received the M.Sc. degree in cartography and hydrology from the Lorand Eötvös University, Budapest, Hungary, the Ph.D. degree from the International Institute for Aerospace Survey and Earth Sciences (ITC), The Netherlands, GIS-based hydrological modelling of alluvial regions (Abstract), defended at ELTE (Summa Cum Laude), in 1996, and the Habilitation degree from Szent István University, Gödöllő, Hungary, in 2015.

He is currently an Assistant Professor with the University of Twente, Enschede, The Netherlands, and a Scientific Advisor with Szent István University. His research interests include satellite hydrology with focus on environmental and agricultural applications.